

Strong anisotropy and its electric tuning for brownmillerite SrCoO_{2.5} films with different crystal orientations

Jinghua Song,^{1,2} Yuansha Chen,^{1,3,*} Hongrui Zhang,^{1,2} Furong Han,^{1,2} Jing Zhang,^{1,2} Xiaobing Chen,^{1,2} Hailin Huang,^{1,2} Jine Zhang,^{1,2} Hui Zhang,^{1,2} Xi Yan,^{1,2} Tahira Khan,^{1,2} Shaojin Qi,^{1,2} Zhihuang Yang,^{1,2} Fengxia Hu,¹ Baogen Shen,¹ and Jirong Sun^{1,4,†}

¹Beijing National Laboratory for Condensed Matter Physics and Institute of Physics, Chinese Academy of Sciences, Beijing 100190, China

²School of Physical Sciences, University of Chinese Academy of Sciences, Beijing 100049, China

³Fujian Institute of Innovation, Chinese Academy of Sciences, Fuzhou, Fujian 350108, China

⁴Songshan Lake Materials Laboratory, Dongguan, Guangdong 523808, China



(Received 9 May 2018; published 4 April 2019)

Brownmillerite oxides (ABO_{2.5}) with long-range ordering of oxygen vacancies own a distinct superstructure formed by alternately stacked octahedral BO₆ and tetrahedral BO₄ planes. The one-dimensional oxygen vacancy channels within BO₄ layers usually lead to high ionic conductivity of brownmillerite oxides, demonstrating great application potential in solid-oxide fuel cells, the oxygen separation membrane, and catalyzers. Here, high quality brownmillerite-SrCoO_{2.5} films have been epitaxially grown on differently oriented substrates by pulsed laser deposition. The anisotropic structural and physical properties of (110)- and (111)-oriented SrCoO_{2.5} films were systematically investigated. We found, unlike the out-of-plane (001)-oriented SrCoO_{2.5} films, the CoO₆ and CoO₄ planes would alternately stack along one of the [100] and [010] axes for (110)-oriented films and one of the [100], [010], and [001] axes for (111)-oriented films, forming coexisting crystal domains with different orientations. More importantly, the superstructure of these films could be reversibly tuned by alternately applying an electric field along two orthogonal directions, switching between an ordered and a disordered state. Corresponding to structural anisotropy, strong in-plane electronic anisotropy of the (110)-oriented SrCoO_{2.5} film was revealed, which was also electrically tunable like the superstructure. This work demonstrates the approaches to modify the ionic conduction channels of brownmillerite oxides, opening avenues towards electrically tunable oxygen separation membrane and catalyzers.

DOI: [10.1103/PhysRevMaterials.3.045801](https://doi.org/10.1103/PhysRevMaterials.3.045801)

I. INTRODUCTION

Transition metal perovskite oxides are typically strong electron-correlated systems showing a variety of interesting effects, such as high- T_c superconductivity, colossal magnetoresistance, ferroelectric polarization, and Mott metal-insulator transitions [1–5]. More importantly, the crystal structure of this kind of complex oxides can be tuned dramatically by the self-doping of oxygen vacancies, exhibiting abundant nonstoichiometric phases [6]. Among them, the brownmillerite (BM) phase has attracted particular attention [7–10] due to its satisfactory performance as an ionic conductor, oxygen separation membrane, catalyzer, and gas sensor [11–14]. BM-structured SrCoO_{2.5} (SCO) is an ideal candidate for the investigation of these unique properties since it is much more stable than its oxygen-rich counterpart SrCoO_{3- δ} at ambient conditions [15–19]. As reported, SCO single crystal is a G-type antiferromagnetic insulator that owns an orthorhombic structure with the lattice constants of $a_o = 5.5739$, $b_o = 5.4697$, and $c_o = 15.7450$ Å [20]. It can be epitaxially grown on suitable perovskite substrates as thin

films on demand, for example on SrTiO₃ (STO, $a = 3.905$ Å) or (LaAlO₃)_{0.3}-(SrAl_{0.5}Ta_{0.5}O₃)_{0.7} (LSAT, $a = 3.868$ Å) [21,22]. When grown on (001)-oriented substrates, pseudotetragonal structured SCO films are formed ($a_t = b_t = 3.905$ Å, and $c_t = 3.936$ Å), with a quadruple superstructure in the [001] direction: Octahedral CoO₆ and tetrahedral CoO₄ planes stack alternately along the out-of-plane direction. Like its bulk counterpart, the BM film is antiferromagnetic and insulating in a wide temperature range. In this kind of thin film, there are one-dimensional (1D) oxygen vacancy channels along the [1 $\bar{1}$ 0] direction, resulting in a high in-plane anionic diffusion [23,24]. When annealed at high temperatures in oxygen atmospheres or gated through ionic liquid, however, the BM film undergoes a phase transition to perovskite structure [25–30]. Accordingly, an antiferromagnetic to ferromagnetic transition takes place, accompanied by an insulator-to-metal transition.

There are intensive investigations in recent years on (001)-oriented SCO films, for which the out-of-plane axis is the direction for superstructure. In contrast, (110)- and (111)-oriented films are scarcely reported. For the (110) and (111) cases, either [100] or [010] or [001] can be the superstructure direction. This introduces two features into the SCO films. The first one is the coexistence of different crystal domains, which provides opportunities for tuning domain structures and related features. The second one is the deviation of the

*Corresponding author: yschen@aphy.iphy.ac.cn

†jrsun@iphy.ac.cn

stacking direction from film normal, which makes it available to investigate the effect of ionic migration across the $\text{CoO}_6/\text{CoO}_4$ planes.

In this paper, we report a systematic study on the anisotropic structural and physical properties of the (110)- and (111)-oriented SCO films. High quality single crystal SCO films have been obtained and their crystal structures are determined. It is found that the CoO_6 and CoO_4 planes stack alternately along one of the [100] and [010] axes for the (110)-oriented films and one of the [100], [010], and [001] axes for the (111)-oriented films, forming coexisting domains with different crystal orientations. Remarkably, the superstructure of the film can be tuned by alternately applying an electric field along two orthogonal directions, reversibly switching between an ordered and a disordered state. Due to structural anisotropy, electronic transport also becomes anisotropic, and is electrically tunable. This work demonstrates the possibility of reversibly modifying the superstructure of BM oxides, opening avenues towards an electrically tunable oxygen separation membrane and catalyzer.

II. EXPERIMENT

High quality BM-SCO thin films with the thickness ranging from 18 to 100 nm were epitaxially grown on (001)-, (110)-, (111)-oriented STO and LSAT substrates ($5 \times 5 \times 0.5 \text{ mm}^3$) by the technique of pulsed laser deposition (KrF, $\lambda = 248 \text{ nm}$). In the deposition process, the substrate was kept at $700 \text{ }^\circ\text{C}$ and the oxygen pressure was set to 12 Pa. The adopted fluence of the laser pulse was 1.1 J/cm^2 and repetition rate was 2 Hz. After deposition, the sample was naturally cooled to room temperature in the same oxygen pressure. The film thickness was determined by the deposition time and the deposition rate is 2 nm/min as has been calibrated by the technique of profile analysis of atomic force microscope (AFM, see Fig. S1 in the Supplemental Material [31]). The

surface morphology of SCO films was measured by AFM (SPI 3800N, Seiko). The crystal structure was determined by a high-resolution x-ray diffractometer (XRD, D8 Discover, Bruker) with the $\text{Cu-K}\alpha$ radiation.

The temperature dependent resistance was measured by a closed cycle refrigerator (CCS-100, Janis) equipped with a Keithley 2611A source meter. Two bar-shaped parallel silver electrodes with a separation of 4 mm were deposited on film surface to investigate the effect of electric tuning. All the electric tuning experiments were performed at room temperature in an air environment. For the determination of electrical anisotropy, the (110)-oriented SCO film was patterned by photolithography and wet etching into two identical Hall bars along the [001] and $[\bar{1}\bar{1}0]$ axes, respectively, with the same length of 3 mm and width of $200 \text{ }\mu\text{m}$ (see Fig. S1 in the Supplemental Material [31]).

III. RESULTS AND DISCUSSIONS

Approximating the BM-SCO phase by a pseudotetragonal structure, the equivalent lattice constants will be $a = b = 3.905 \text{ \AA}$ and $c = 3.936 \text{ \AA}$. Obviously, the (001)-oriented SCO film has good lattice matching with STO but a fairly large lattice mismatch (-1%) with LSAT. Figure 1 compares the surface morphology of as-grown SCO films on STO or LSAT substrates with different orientations. A very smooth surface and highly preferential growth of crystalline grains can be clearly seen in the (001)- and (110)-oriented films, whereas the surface morphology of (111)-oriented films are relatively rough. The root-mean-squared roughness (RMS) is $\sim 0.34 \text{ nm}$ for (001)-, $\sim 0.47 \text{ nm}$ for (110)- and $\sim 2.2 \text{ nm}$ for (111)-oriented SCO/STO films (40 nm in thickness). For the SCO films on LSAT (40 nm in thickness), the corresponding parameters are ~ 0.62 , ~ 0.95 , and $\sim 2.1 \text{ nm}$.

In order to determine the crystal structure of SCO films, XRD spectra were collected for the lattice planes parallel to

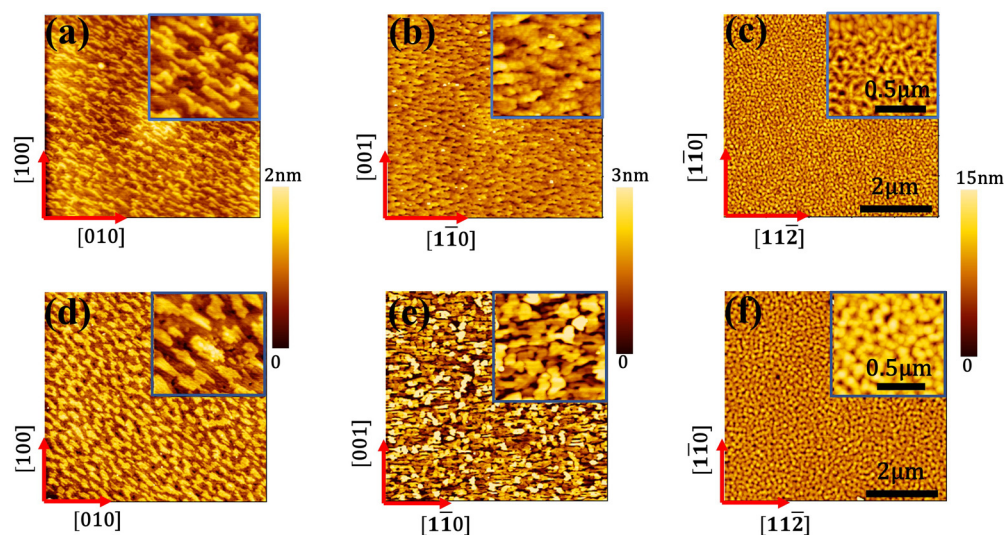


FIG. 1. (a)–(c) AFM images ($5 \text{ }\mu\text{m} \times 5 \text{ }\mu\text{m}$) of SCO films grown on (001)-, (110)- and (111)-oriented STO substrates, respectively. (d)–(f) AFM images ($5 \text{ }\mu\text{m} \times 5 \text{ }\mu\text{m}$) of SCO films grown on (001)-, (110)-, and (111)-oriented LSAT substrates. The thickness of all films is 40 nm. Insets are enlarged images over an area of $1 \text{ }\mu\text{m} \times 1 \text{ }\mu\text{m}$. Corresponding results for 18 and 100 nm films are given in Fig. S2 of the Supplemental Material [31].

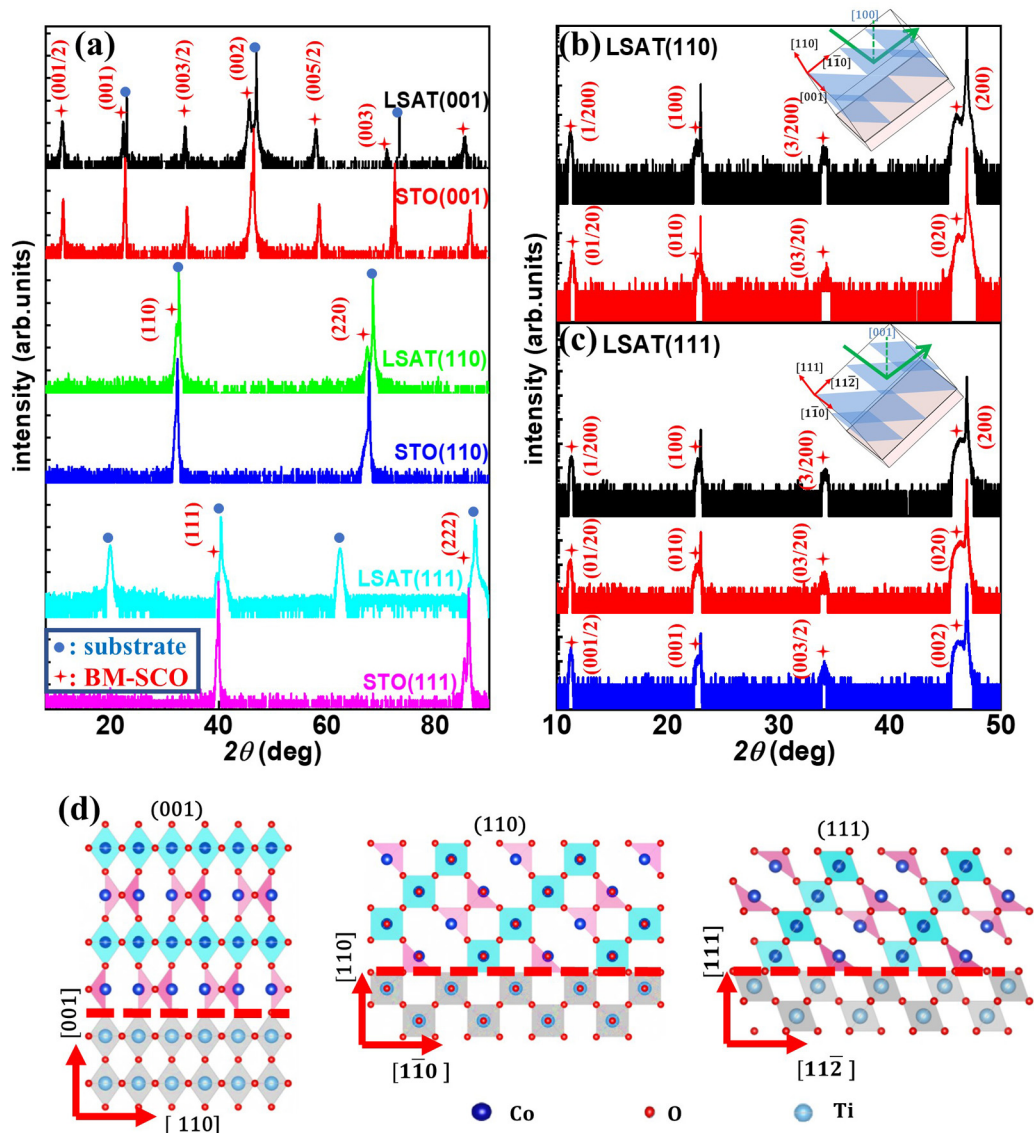


FIG. 2. (a) XRD spectra of the lattice planes parallel to film surface for the SCO epitaxial films (40 nm in thickness) with the (001), (110), and (111) orientations, indexed in the perovskite structure. Reflections with half integer indices indicate the formation of the superstructure along the [001] direction for the (001)-oriented film. (b) XRD spectra of the (110)-oriented SCO/LSAT film, reflected from the (100) and (010) lattice planes (black and red patterns). Satellite peaks indicate the formation of superstructure along the [100] or [010] direction. (c) XRD spectra of the (111)-oriented SCO/LSAT film, reflected from the (100), (010), and (001) lattice planes (black, red, and blue patterns). For clarity, XRD spectra have been shifted upwards by different distances. (d) Schematics of the superstructure of the (001)-, (110)-, and (111)-oriented SCO films; here Sr atoms have been dropped for clarity. The blue and pink polyhedrons refer to the octahedral CoO₆ and tetrahedral CoO₄, respectively

film plane. Figure 2(a) shows the XRD patterns of the (001)-, (110)-, and (111)-oriented films with the same thickness of 40 nm, reflected from the lattice planes parallel to film surface (see Fig. S4 in the Supplemental Material [31] for the enlarged images of {002} peaks). Typical features of the BM phase are observed in (001)-oriented SCO films: In addition to the expected (00l) reflections, a series of satellite peaks with the indices of $(00\frac{l}{2})$ are clearly seen. The deduced out-of-plane lattice constant is 3.971 Å for SCO/LSAT and 3.934 Å for SCO/STO, similar to the reported values for the respective films [26,29]. As well established, the CoO₆ and CoO₄ planes stack alternately along the out-of-plane direction, forming a quadruple superstructure. Since the SCO/LSAT film suffers

from strong compressive in-plane strains, its out-of-plane lattice parameter is considerably large. These results confirm the formation of BM-structured (001)-oriented SCO films.

Different from the (001)-oriented film, satellite peaks are not observed for the (110)- and (111)-oriented films though $(hh0)$ and (hhh) reflections are clearly seen [Fig. 2(a)]. This result means that superstructure, if it forms, does not align along the out-of-plane direction. On the analogy of (001)-oriented films, alternate CoO₄/CoO₆ stacking will appear only along one of the [100], [010] and [001] axes. Taking the (110)-oriented film as an example, either the [100] or [010] axis could be the stacking direction; here the in-plane [001] axis is ruled out since it will cause a compression of the

superstructure. For a collection of the Bragg reflections of the [100] planes, we rotated the film counterclockwise around the [001] axis by $\sim 45^\circ$ and performed the θ - 2θ scanning. Figure 2(b) presents the XRD spectra thus obtained in the (110)-oriented SCO/LSAT film [Similar data for (110)-oriented SCO/STO films are shown in Fig. S3(a) of the Supplemental Material [31]]. Indeed, satellite peaks with the indices of $(\frac{h}{2}00)$ are observed. When rotating the film clockwise around the same axis by $\sim 45^\circ$, another series of $(0\frac{k}{2}0)$ peaks appear. These results indicate that the BM phase is also formed in the (110)-oriented film but the stacking direction deviates from the film normal by an angle of $\sim 45^\circ$. Moreover, two kinds of crystal domains with respective to the [100] and [010] orientations coexist in the (110) film. Based on the half integer peaks in the XRD spectra, the averaged lattice constant along the stacking direction can be obtained. It is 3.944 and 3.937 Å for (110)-oriented SCO/LSAT and SCO/STO films (40 nm), respectively.

Similarly, the XRD spectra of the (100), (010), and (001) planes for the (111)-oriented films can be obtained [see Fig. 2(c) for the LSAT substrate and Fig. S3(b) in the Supplemental Material [31] for STO substrate]. As expected, either of the three axes can be the stacking direction. The deduced lattice constant along the stacking direction is 3.950 Å for the (111)-oriented SCO/LSAT and 3.948 Å for the (111)-oriented SCO/STO (40 nm in thickness). Similar to the (110)-oriented films, the (111)-oriented films are not singly domain structured either. To get a clear picture on the superstructure of differently oriented films, Fig. 2(d) presents sketches for the epitaxial growth of (001)-, (110)-, and (111)-oriented SCO films on STO substrates, from which the stacking directions can be clearly seen.

In addition to the lattice constant along the stacking direction, more lattice parameters are required to describe the crystal structure of our SCO films. As reported, the (001)-oriented SCO film is tetragonal, and its two orthogonal in-plane lattice constants are the same as those of the substrate, i.e., $a = b = 3.905$ Å (for SCO/STO) or 3.868 Å (for SCO/LSAT) [29]. In order to get the complete lattice parameters of the (110)- and (111)-oriented SCO films, the reciprocal space mappings (RSMs) for selective Bragg reflections are collected. Figures 3(a) and 3(b) are RSMs of the (222) and (130) reflections of a (110)-oriented SCO/STO film (40 nm in thickness), respectively. The split substrate peaks indicate that the STO substrate is not a high-quality single crystal [32]. Though this will result in a somewhat uncertain lattice parameters (see Fig. S5 in the Supplemental Material [31]), fortunately, the overall structural feature of BM-SCO films will not be affected. An elliptic diffraction peak of the film (marked by a cross) is observed in each case, just below that of the substrate. It means that the SCO film has the same in-plane lattice parameter as the substrate, i.e., $c = 3.905$ Å and $D[1\bar{1}0] = 5.522$ Å ($D[1\bar{1}0]$ is the nearest-neighbor distance of Sr-Sr ions along the $[1\bar{1}0]$ direction, i.e., the line segment that links lattice sites (1,0,0) and (0,1,0) of SCO as labeled in Fig. S5 of the Supplemental Material [31]). In contrast, the out-of-plane $d_{(110)}$ is slightly larger than that of the substrate (2.791 Å versus 2.761 Å). Taking the a -oriented domain as an example (the stacking direction is along [100] axis), from the

deduced values of $D[1\bar{1}0]$, $d_{(110)}$, and a , the lattice parameters of $b = 3.913$ Å and $\gamma = 89.34^\circ$ are obtained after simple calculations [refer to Fig. 3(c) for the relations between lattice parameters and Fig. S5 of the Supplemental Material [31] for detailed calculations]. The deduced lattice parameters for the (110)-oriented SCO/STO film are tabulated in Table I. Notably, the lattice constants are comparable to those of (001)-oriented SCO/STO films.

RSMs are also recorded for the (110)-oriented SCO/LSAT films. Different from (110)-oriented SCO/STO, the (110)-oriented SCO/LSAT films show considerable lattice relaxations. As shown in Fig. 3(d), the (222) peak splits into two spots along the [110] direction, an intensive one and a weak one near and away from the corresponding peak of the substrate, respectively. This result implies the occurrence of two SCO phases. We note that, in the [001] direction, the first phase shares the same $c = 3.868$ Å with substrate, whereas the second phase shows the c -axis lattice constantly growing from 3.877 to 3.901 Å with film thickness increases from 18 to 100 nm. In contrast, lattice relaxation along the $[1\bar{1}0]$ direction takes place in both phases, as illustrated by the RSM of (040) reflection [see Fig. 3(e) and Fig. S6 in the Supplemental Material [31]]. In other words, the first phase is fully strained in the c axis whereas the second phase is free in either the [001] or $[1\bar{1}0]$ direction. A natural assumption is that the first phase is a near interface phase, suffering from the clamping of the substrate [33,34]. The second phase may be formed in the proximity of film surface and lattice relaxation, and is relatively easy. The large lattice mismatch between BM-SCO and LSAT (-1%) could be the reason for the formation of two layered phases. A similar phenomenon has been reported for a thick $\text{Nd}_{0.5}\text{Sr}_{0.5}\text{MnO}_3$ film grown on a LaAlO_3 substrate, showing a strained and a relaxed phase [35]. From the data in Figs. 3(d) and 3(e), $D[1\bar{1}0]$ and $d_{(110)}$ can be deduced. Following the same procedure as for SCO/STO, other lattice parameters are gained for each phase (Table I). It is worth noting that the unit cell volume of the strained phase has an average value of ~ 0.0589 nm³ that is close to the fully strained (001)-oriented SCO/LSAT film (~ 0.0594 nm³). Differently, the unit cell volume of the relaxed phase demonstrates a sustained expansion with film thickness, from 0.0597 nm³ for the 18-nm film to 0.0606 nm³ for the 100nm film. Its average value (~ 0.0602 nm³) is closer to the strain-free (001)-oriented SCO/STO films or SCO bulk crystal (~ 0.0600 nm³).

For the (111) SCO/STO film, we selected the (132) reflection on the $[111]$ - $[1\bar{1}0]$ plane and the (114) reflection on the $[111]$ - $[1\bar{1}\bar{2}]$ plane. Interestingly, two separated peaks aligned along the $[1\bar{1}0]$ or the $[1\bar{1}\bar{2}]$ direction are observed [Figs. 3(f) or 3(g)]. This peak splitting cannot be ascribed to lattice relaxation since both peaks have the same $d_{[111]}$ value. A further analysis suggests that they stem from c - and a -oriented (or b -oriented) domains, respectively (see Fig. S5 in the Supplemental Material [31]). As shown in Fig. 3(h), the $D[1\bar{1}0]$ (or $D[1\bar{1}\bar{2}]$) value is slightly smaller (or larger) for c -oriented domains than for a - and b -oriented domains. Since the a - and b -oriented domains have the same peak position whereas the c -oriented domain does not, the intensity ratio of these two peaks is approximately 2:1. After a direct

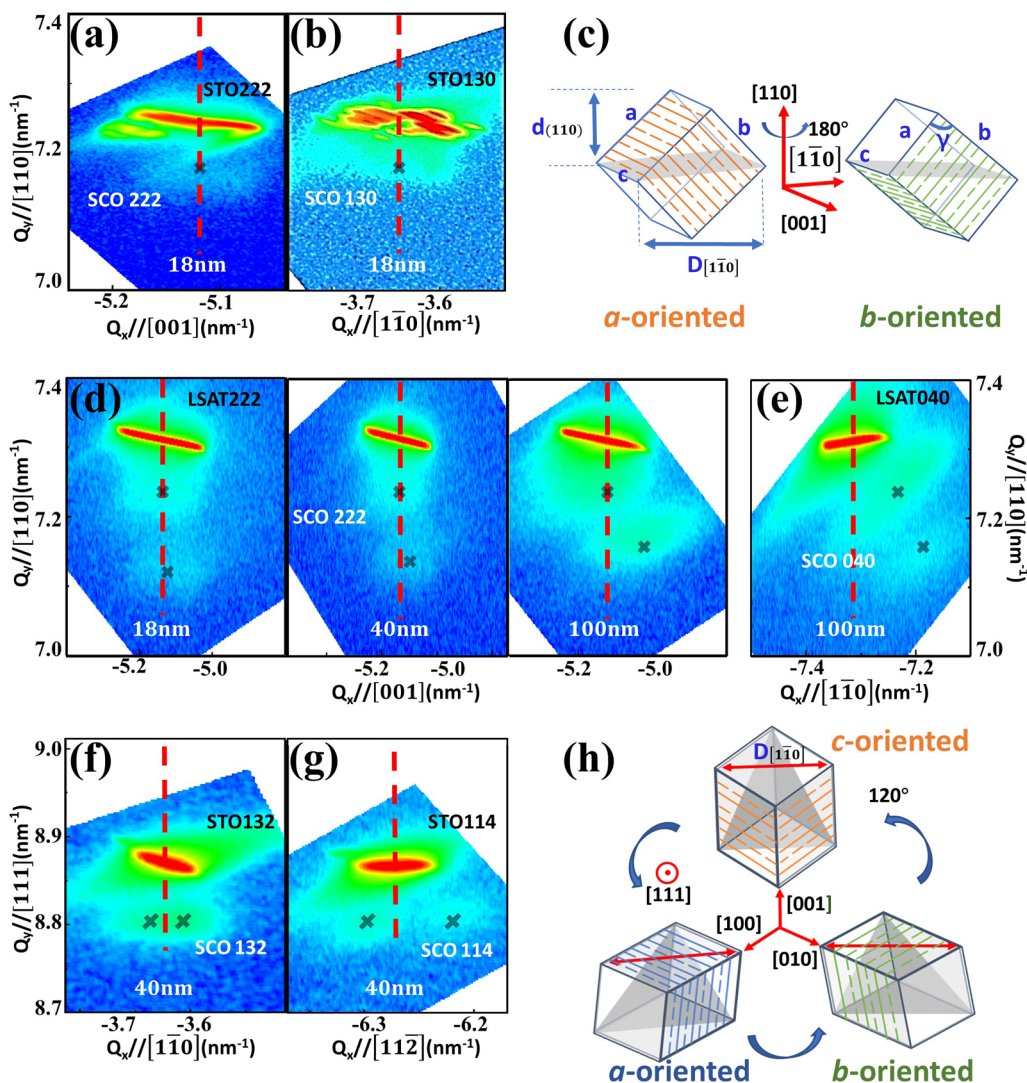


FIG. 3. (a) and (b) Respective RSMs of the (222) and (130) reflections for the (110)-oriented SCO/STO film. Film thickness is 18 nm. (c) A schematic diagram for the twofold domain structure of the (110)-oriented SCO film. The solid and dashed lines indicate the alternately stacked CoO_6 and CoO_4 layers. (d) RSMs of the (222) reflections of the (110)-oriented SCO/LSAT films, showing two separated peaks along the [110] direction. The film thickness is 18 nm (left), 40 nm (middle) or 100 nm (right), respectively. (e) RSM around the (040) LSAT reflection of the 100 nm (110)-oriented SCO film. (f) and (g) RSMs around (132) and (114) for the (111)-oriented SCO/STO film (40 nm). (h) Schematic model for the threefold domain structure of (111)-oriented SCO films.

calculation based on the deduced values of $d_{(111)}$, $D[1\bar{1}0]$, $DD[01\bar{1}]$, and a , the lattice parameters of the a -oriented domains for (111) film can also be determined (Table I). Peak splitting is also observed in (111) SCO/LSAT films (see Fig. S7 in the Supplemental Material [31]). Different from (110) SCO/LSAT, however, no phase separation appears here. This is understandable since the lattice stress in (111) SCO/LSAT could be more easily released without the clamping from the substrate to the a -, b -, and c -axes. According to Table I, the (110)- and (111)-oriented films are slightly monoclinic, unlike the tetragonal (001)-oriented film. Moreover, the stacking direction of CoO_4 and CoO_6 planes along the $[100]/[010]$ axis for the (110)-oriented film and the $[100]/[010]/[001]$ axis for the (111)-oriented film, deviating from film normal. This, as will be shown below, provides us opportunities to tune the superstructure of the film via in-plane electric fields.

As well established, for the BM-structured oxides it is relatively easy for an electric field to drive an anionic migration. When the oxygen drift takes place in the direction across the CoO_4 and CoO_6 planes, it is expected to cause a mixture of these two kinds of planes, thus a variation of the conduction channels for oxygen vacancies. This implies an electric tuning to the migration channels for oxygen anions. (110)-oriented SCO films provide a promising playground for the investigation of this effect. In order to induce an anionic migration, we applied an electric field to the SCO films along the $[1\bar{1}0]$ direction and observed obvious changes in both surface morphology and crystal structure. Figure 4(a) shows the typical topographies of the (110)-oriented SCO/LSAT film, recorded at different stages of electric biasing. The film is initially smooth with an average grain size of ~ 200 nm. After two successive 500-s applications of an electric bias of 200 V (electric field strength of 500 V/cm), considerable fine

TABLE I. Lattice parameters of a -oriented domains in (110) and (111) SCO films, where α , β , γ are the angles between the b and c , a and c , a and b axes, respectively

Substrate	Thickness	Phase	A (Å)	b (Å)	c (Å)	α (deg)	β (deg)	γ (deg)
LSAT(110)	18 nm	Strained	3.930	3.863	3.868	90	90	89.53
		Relaxed	3.969	3.882	3.877	90	90	88.85
LSAT(110)	40 nm	Strained	3.932	3.873	3.868	90	90	89.81
		Relaxed	3.970	3.881	3.886	90	90	89.02
LSAT(110)	100 nm	Strained	3.944	3.870	3.868	90	90	90.01
		Relaxed	3.987	3.898	3.901	90	90	89.71
STO(110)	40 nm	Strained	3.937	3.913	3.905	90	90	89.34
STO(111)	40 nm	Strained	3.948	3.899	3.899	90.22	90.17	90.17

grains form [from step 0 to 2 in Fig. 4(a)], dispersing on the surface of coarse grains. This is an indication of the variation of SCO film after electrical processing. Fascinatingly, the biasing effect is reversible: the initial topography recovers after turning over the bias polarity (from step 3 to 4). The biasing effect can also be identified from the RMS of film surface, which increases from 0.95 to 1.05 nm under positive biases and goes back to 0.96 nm under subsequent negative biases. Accordingly, the resistance in the $[1\bar{1}0]$ direction displays a reversible variation [Fig. 4(b)]. Corresponding to these changes, the superstructure of the (110)-oriented film undergoes a dramatic transformation. Figure 4(c) presents $(\frac{1}{2}00)$ and $(0\frac{1}{2}0)$ reflections in as-prepared, positively biased and negatively biased states, respectively. A clear satellite peak is observed for the as-prepared film, specifying the well-ordered BM superstructure. The peak intensity gradually decreases with biasing time and nearly completely vanishes after 1000 s. Both the a - and b -oriented domains are modified by electric field. Under reversing bias, the superstructure peak reappears, restoring $\sim 80\%$ of its initial intensity after 1000 s. Corresponding changes in (200) integer peaks are shown in Fig. S8(a) of the Supplemental Material [31], which demonstrate a similar tendency to half integer peaks but reduced degree of changes.

Obviously, not only morphology but also crystal structure of the SCO film suffers from the biasing effect. When biasing time is long enough (>2000 s), however, the electric effect becomes irreversible. Rather than returning to its initial state, the film structure is much more disordered under reversed biases, as indicated by the appearance of scaly-type grains [see step 2 in Fig. 4(d) and Fig. S8 in the Supplemental Material [31]] and the disappearance of half-order reflections [step 2 in Fig. 4(e)]. It is obvious that the reversed biases cannot rebuild the superstructure when the structure is far from its initial state. Surprisingly, an electric field along $[001]$ direction has a distinct effect that rebuilds the superstructure. Under this field, the scaly-type grains gradually disappear and, finally, the initial film surface recovers [(steps 3 and 4 in Fig. 4(d)]. Correspondingly, superstructure peaks emerge and develop [steps 3 and 4 in Fig. 4(e)]. This phenomenon is repeatable, observed when we repeat the electric cycling alternately along the $[1\bar{1}0]$ and $[001]$ directions.

Half-order peaks are closely related to the superstructure of the SCO film. Their disappearance indicates the disor-

dering of CoO_4 and CoO_6 planes. As reported, it is easy for oxygen anions to migrate along the CoO_4 planes. This means that an electric field applied along the $[1\bar{1}0]$ axis will cause an anionic drift along this direction, i.e., an oxygen migration across the $\text{CoO}_6/\text{CoO}_4$ planes. This drift could be nonuniform, and an interlacing of the CoO_4 and CoO_6 planes may take place, breaking the long-range order of the superstructure [Fig. 4(f)]. If the distance for anionic migration is short (in the range of tens to hundreds of nanometers), the fragmentary CoO_4 (CoO_6) planes may integrate together after the backward shift of the oxygen anions under reversed biases, rebuilding the superstructure. This explains the reversible electric tuning effect when biasing time is not too long (<1000 s). However, if the migration distance is long enough (several μm s), reverse biases are unable to drive the oxygen atoms to where they were. On the contrary, they make the arrangement of the CoO_4 - CoO_6 planes further disordered. It is an interesting observation that an electric field along the $[001]$ axis re-establishes the superstructure. Possibly, the oxygen migration in this direction causes a position exchange for misplaced CoO_4 and CoO_6 planes, driving them into an ordered state. This is understandable considering that the intertwining of the CoO_4 and CoO_6 planes could be disfavored due to its resistance to anionic conduction along the $[001]$ direction.

As well documented, the diffusion coefficient of lattice oxygen of SCO is $\sim 10^{-12}$ cm^2/s at room temperature [36]. Based on this result, the migration distance of oxygen anions/vacancies under the electric field of 500 V/cm can be directly estimated, and it is ~ 200 nm for a tuning time of ~ 1000 s and ~ 2 μm for a tuning time of ~ 10000 s. According to Figs. 4(a) and 4(d), the grain size is ~ 0.5 μm for SCO/LSAT and ~ 1 μm for SCO/STO. Notably, concentrated fine particles appear on grain surface when drift distance is close to and exceeds the grain size. This is understandable since in this case inner anions have opportunities to reach the grain surface. According to our experimental results, the time scales for destroying and rebuilding the superstructure are of the same order. This is reasonable because both processes are closely associated with the migration of oxygen vacancies. Noting the fact that the ordering of oxygen vacancies forms the conduction channels for oxygen anions, the biasing effect on the superstructure implies an electric tuning of ionic conduction. This finding is important in a sense that it suggests an approach to reversibly modifying the performance

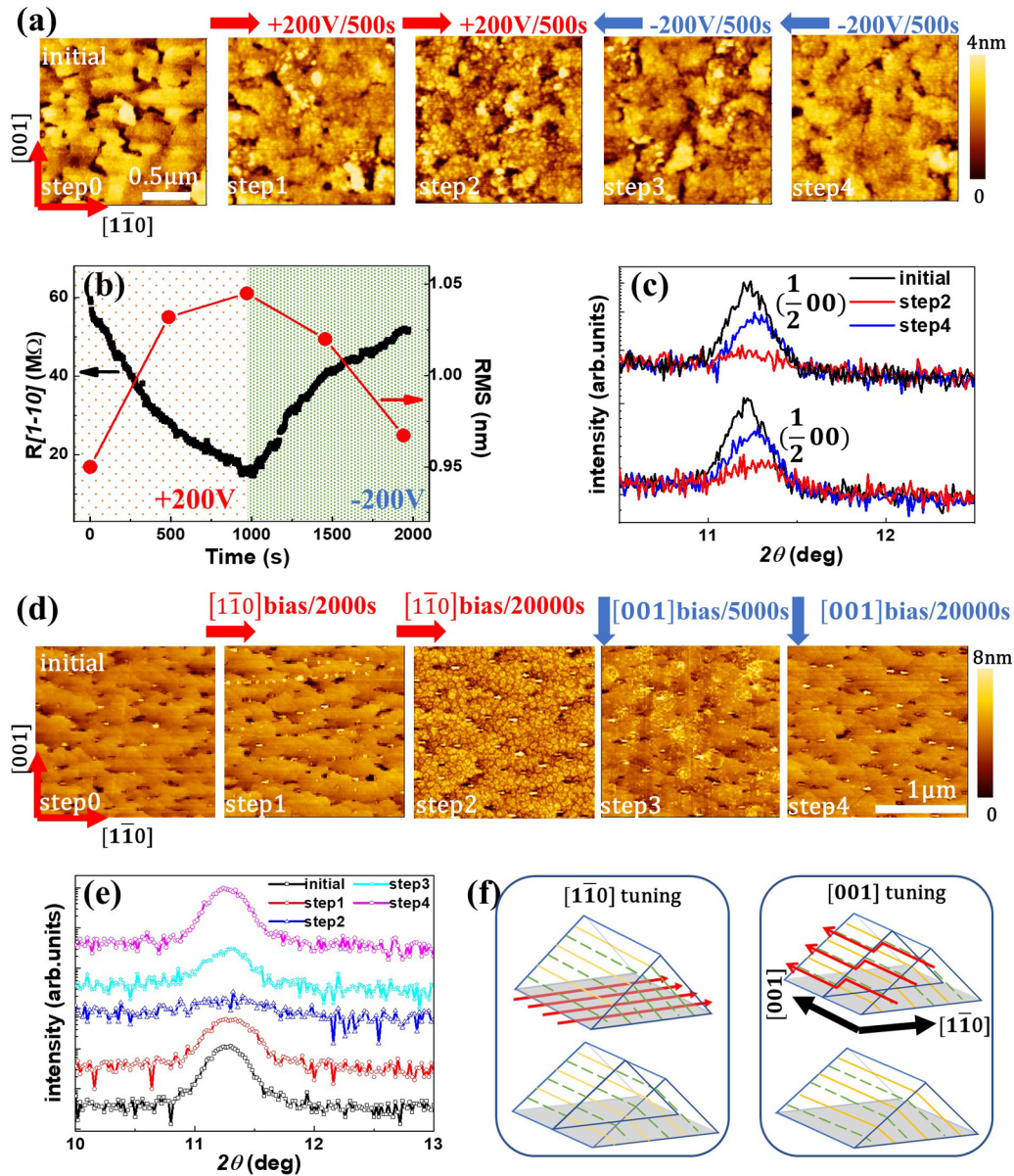


FIG. 4. (a) Surface morphology of the (110)-oriented SCO/LSAT film with a thickness of 40 nm, recorded before and after electric tuning. Step 0 corresponds to the initial state. Steps 1 to 4 correspond to different stages during the biasing processes. Here the electric field is applied along the $[1\bar{1}0]$ direction. Voltage is 200 V and the distance between electrodes is 4 mm. Arrows mark the direction of electric field. (b) Variation of $R[1\bar{1}0]$ and RMS during the biasing process. (c) Superstructure peaks of the (110) SCO/LSAT film, obtained in differently biased states. The top and bottom spectra correspond to a - and b -oriented domains, respectively. (d) Surface morphology of the (110) SCO/STO film (40 nm) in differently biased states. Arrows mark the direction of electric field. Voltage is 200 V and the distance between electrodes is 4 mm. The result of (110) SCO/LSAT film is shown in Fig. S9 of the Supplemental Material [31]. (e) The $(\frac{1}{2}00)$ peak in differently biased stages corresponding to the morphologies in (d). (f) A schematic diagram of the anisotropic biasing effect on resistance, surface morphology, and superstructure. Left: inhomogeneous migration of oxygen vacancies along the $[1\bar{1}0]$ direction splits the large grain into small pieces. Right: $[001]$ bias tuning realigns the $\text{CoO}_6/\text{CoO}_4$ layers and rebuilds the superstructure. The AFM images at different tuning states are not obtained from exactly the same area. However, we measured different areas at each stage of the electric tuning and observed very similar morphologies (see Fig. S10 in the Supplemental Material [31]). All experiments were performed in air environment.

of the BM-type oxide as ionic conductors, oxygen separation membranes, and catalyzers.

In addition to anionic conduction, electronic transport, which is expected to be anisotropic due to structural anisotropy, can also be tuned by electric field. Figure 5(a) is a schematic view of two identical Hall bars along the $[001]$ and $[1\bar{1}0]$ axes, respectively. In Fig. 5(b) the I - V curve

of these two Hall bars are shown. For the SCO/LSAT film, the resistance along the $[1\bar{1}0]$ axis ($R[1\bar{1}0]$) is nearly two orders of magnitude higher than that along the $[001]$ axis ($R[001]$). For the SCO/STO film, although the $R[1\bar{1}0]/R[001]$ ratio is slightly smaller, it is still as large as 10. According to Fig. 3(c), the $[001]$ axis is parallel to the $\text{CoO}_6/\text{CoO}_4$ planes. It is an ionic conduction channel and also could be a

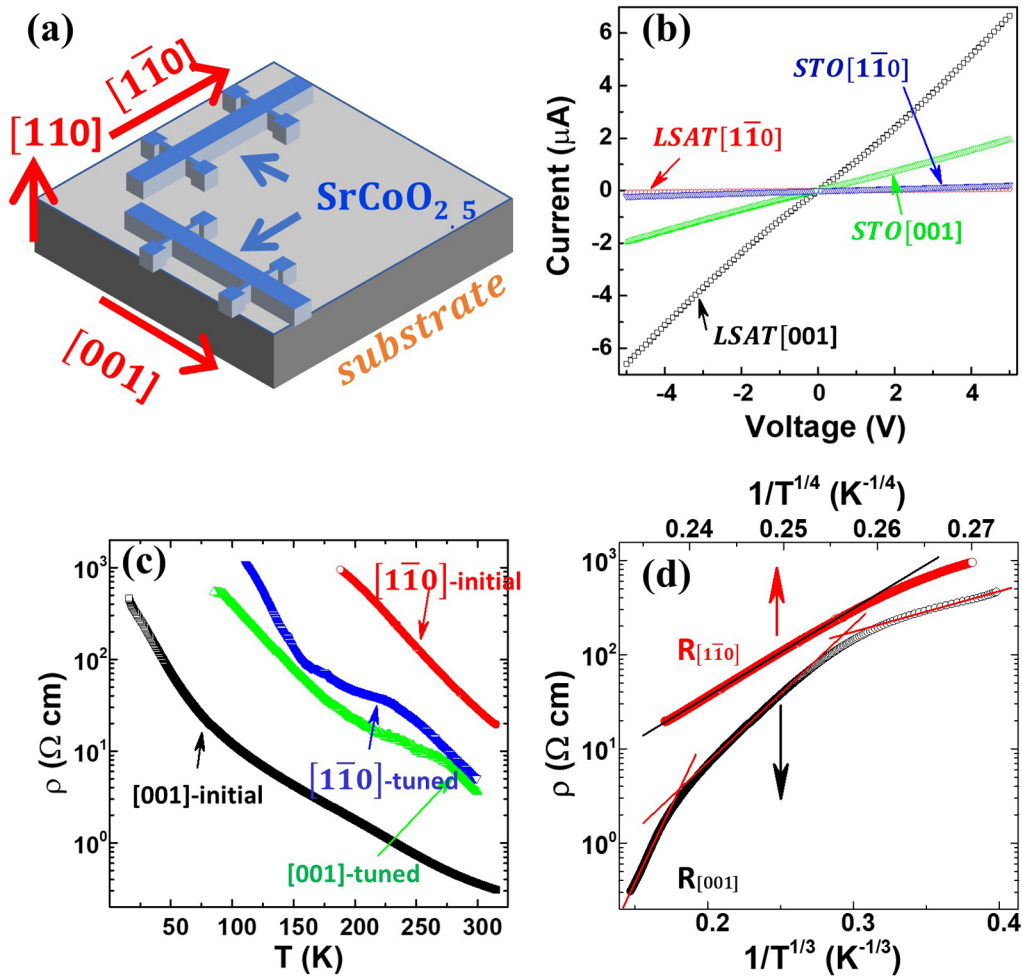


FIG. 5. (a) A schematic view of the patterned SCO bars. (b) I - V curves of the (110) -oriented SCO films (40 nm) grown on STO and LSAT, measured along the two in-plane directions $[001]$ and $[1\bar{1}0]$. $R_{[001]}/R_{[1\bar{1}0]}$ is ~ 100 for SCO/LSAT and ~ 10 for SCO/STO. (c) Resistivity as a function of temperature, measured along the $[001]$ and $[1\bar{1}0]$ directions for ordered and disordered (110) -oriented SCO/LSAT films (40 nm). The electrical anisotropy is depressed by an electric biasing of 200 V \oplus 20000 s along the $[1\bar{1}0]$ direction (Electrode separation is 4 mm). The temperature-dependent resistivity of (110) -oriented SCO/STO film is given in Fig. S11 of the Supplemental Material [31]. (d) Semilogarithmic plot of the resistivity of (110) -oriented SCO/LSAT film along the $[001]$ and $[1\bar{1}0]$ directions versus $1/T^{1/3}$ or $1/T^{1/4}$, respectively. Solid lines are guides for the eye.

channel for electronic transport noting that the CoO_6 network in SrCoO_3 is metallic. In contrast, the conduction along the $[1\bar{1}0]$ direction proceeds across the $\text{CoO}_4/\text{CoO}_6$ planes, thus it is much more difficult because the CoO_4 planes are highly insulating [28,29]. According to Fig. 5(b), the resistance along the $[001]$ direction is considerably smaller for the SCO film on LSAT than on the STO substrate. It could be a consequence of different lattice strains in these two films. A direct calculation indicates that the lattice strain along the $[001]$ direction is -1% for SCO/LSAT and ~ 0 for SCO/STO, adopting the pseudotetragonal lattice parameter of SCO. In general, compressive strains favor a high conductance, due to the enhanced overlap of electron orbits [37,38].

A further analysis of the $R_{[001]}-T$ dependence shows that the conduction along the $[001]$ axis proceeds in the form of a 2D variable range hopping (VRH), i.e., $R_{[001]} \propto \exp(T_0/T^{1/3})$, where T_0 is a constant independent of temperature [Fig. 5(d)]. As mentioned above, the metallic CoO_6 planes of the (110) SCO films are always parallel to the $[001]$

axis for either a -oriented or b -oriented domains, thus resulting in much lower resistivity of $R_{[001]}$ compared with $R_{[1\bar{1}0]}$. Moreover, since the CoO_6 plane is separated by insulating CoO_4 planes, the electronic conduction along this plane is 2D in nature. Different from $R_{[001]}$, $R_{[1\bar{1}0]}$ is proportional to $\exp(T_0/T^{1/4})$, indicating a 3D VRH. Notably, the conduction proceeds in the form of VRH rather than the conventional short-range hopping [$R \propto \exp(-E/k_B T)$], which usually appears in band semiconductors and disordered electron systems, where E is the activation energy and k_B is the Boltzmann constant. This implies that the electrons in the SCO film are strongly localized. In this case, electron hopping takes places between sites with similar energies but is variably separated [39,40]. There are two obvious inflections at ~ 60 and ~ 195 K, respectively, in the $R_{[001]}-T$ dependence, resulting in three electronic processes [Fig. 5(d)]. This result indicates that the SCO film experiences different electronic states with the decrease of temperature. At present, the underlying mechanisms that leads to these two transitions are still not clear. A

similar transition of the hopping conduction upon cooling at low temperature has been observed in insulating manganite and ascribed to the formation of antiferromagnetic transition [41]. In the manganite, experiencing a charge ordering transition, the R - T dependence, like the one observed here around 170 K, is reported [42]. Magnetic transition or charge ordering in SCO film cannot be completely ruled out when cooled below room temperature and deserves further investigations.

Similar to ionic conduction, the electronic transport also suffers from the electric tuning effect. Figure 5(c) presents the temperature dependence of the resistivity (ρ) of the SCO/LSAT film, obtained before and after a process of electric biasing along the $[1\bar{1}0]$ direction. Accompanying structural disordering, the two ρ - T curves acquired along the $[001]$ and $[1\bar{1}0]$ directions become close to each other, indicating a weakening of the resistive anisotropy. Taking the resistance at room temperature for example, $R_{[001]}$ is increased by a factor of ~ 12 after an electric tuning of 2000 s. In contrast, $R_{[1\bar{1}0]}$ is reduced by a factor of ~ 3 . The dramatic increase in $R_{[001]}$ implies that, when viewed along the $[001]$ axis, the conducting CoO_6 planes become incomplete now, as a consequence of the embedment of fragmented CoO_4 planes in CoO_6 planes. As stated above, electrically biasing the SCO film along the $[1\bar{1}0]$ direction is expected to cause a parallel translation of the vertical CoO_6 and CoO_4 planes in this direction. However, a rigid shift of the whole plane is impossible since the ionic mobility may vary from location to location. As a consequence, the CoO_6 and CoO_4 planes will interlace with each other, resulting in CoO_6 and CoO_4 mixed lattice planes. The decrease of $R_{[1\bar{1}0]}$ is understandable since the resistive CoO_4 planes, across which the electronic transport along $[1\bar{1}0]$ direction proceeds, are incomplete after electrical processing. Obviously, the effects of mixing the CoO_6 and CoO_4 planes are different on the conduction along $[001]$ and $[1\bar{1}0]$ directions.

IV. CONCLUSION

In summary, high-quality BM-structured SCO films with different orientations are fabricated, and their crystal structures are determined. All films show superstructure, due to an alternate stacking of the CoO_4 and CoO_6 planes. Different from (001)-oriented films for which out-of-plane stacking is observed, the superstructure appears along either the $[100]$ or the $[010]$ axis for (110)-oriented films and either the $[100]$ or the $[010]$ or the $[001]$ axis for (111)-oriented films, forming an angle with the out-of-plane direction. For the (110)-oriented film, furthermore, the dramatic tuning of an in-plane electric field to superstructure and thus to anionic conduction channels is demonstrated. The film reversibly switches between a structurally ordered and a disordered state as the electric field is applied alternately along two orthogonal directions. Due to the structural anisotropy, strong in-plane electronic anisotropy of (110)-oriented SCO film is demonstrated, which is also electrically tunable like ionic conduction. This work reveals the approaches to modify the superstructure and further tailor the oxygen vacancy channels of BM oxides, opening avenues to develop electrically tunable oxygen separation membranes and catalyzers.

ACKNOWLEDGMENTS

This work has been supported by the National Basic Research of China (No. 2016YFA0300701, No. 2017YFA0206300, and No. 2017YFA0303601), the National Natural Science Foundation of China (No. 11520101002, No. 51590880, and No. 11674378), and the Key Program of the Chinese Academy of Sciences and State Key Laboratory of Advanced Technology for Materials Synthesis and Processing (Wuhan University of Technology). We also acknowledge Beamline BL08U1A in the Shanghai Synchrotron Radiation Facility (SSRF) for the surface characterizations.

-
- [1] A. Umezawa, W. Zhang, A. Gurevich, Y. Feng, E. E. Hellstrom, and D. C. Larbalestier, *Nature (London)* **364**, 129 (1993).
 - [2] J.-H. Park, E. Vescovo, H.-J. Kim, C. Kwon, R. Ramesh, and T. Venkatesan, *Nature (London)* **392**, 794 (1998).
 - [3] S. S. Rao, J. T. Prater, F. Wu, C. T. Shelton, J.-P. Maria, and J. Narayan, *Nano Lett.* **13**, 5814 (2013).
 - [4] Y. Tokura, Y. Taguchi, Y. Okada, Y. Fujishima, and T. Arima, *Phys. Rev. Lett.* **70**, 2126, (1993).
 - [5] F. Trier, G. E. D. K. Prawiroatmodjo, Z. Zhong, D. V. Christensen, M. von Soosten, A. Bhowmik, J. M. G. Lastra, Y. Chen, T. S. Jespersen, and N. Pryds, *Phys. Rev. Lett.* **117**, 096804 (2016).
 - [6] Y. Matsumoto, S. Yamada, T. Nishida, and E. Sato, *J. Electrochem. Soc.* **127**, 2360 (1980).
 - [7] A. Piovano, M. Ceretti, M. R. Johnson, G. Agostini, W. Paulus, and C. Lamberti, *J. Phys.: Condens. Mater.* **27**, 225403, (2015).
 - [8] S. Inoue, M. Kawai, N. Ichikawa, H. Kageyama, W. Paulus, and Y. Shimakawa, *Nat. Chem* **2**, 213 (2010).
 - [9] B. C. H. Steele, *Mater. Sci. Eng. B* **13**, 79 (1992).
 - [10] E. Sullivan and C. Greaves, *Mater. Res. Bull.* **47**, 2541 (2012).
 - [11] J. Scholz, M. Risch, G. Wartner, C. Luderer, V. Roddatis, and C. Jooss, *Catalysts* **7**, 139 (2017).
 - [12] J. H. Kim, S.-W. Baek, C. Lee, K. Park, and J. Bae, *Solid State Ionics* **179**, 1490 (2008).
 - [13] E. Bakken, T. Norby, and S. Stolen, *J. Mater. Chem.* **12**, 317, (2002).
 - [14] V. L. Kozhevnikov, I. A. Leonidov, M. V. Patrakeev, and E. B. Mitberg, *J. Solid State Chem.* **158**, 320 (2001).
 - [15] G. H. Jonker and J. H. Vansanten, *Physica* **19**, 120 (1953).
 - [16] T. Takeda, H. Watanabe, and Y. Yamaguchi, *J. Phys. Soc. Jpn.* **33**, 970 (1972).
 - [17] R. L. Toquin, W. Paulus, A. Cousson, C. Prestipino, and C. Lamberti, *J. Am. Chem. Soc* **128**, 13161 (2006).
 - [18] A. Nemudry, P. Weiss, I. Gainutdinov, V. Boldyrev, and R. Schollhorn, *Chem. Mater.* **10**, 2403 (1998).
 - [19] A. Piovano, G. Agostini, A. I. Frenkel, T. Bertier, C. Prestipino, M. Ceretti, W. Paulus, and C. Lamberti, *J. Phys. Chem. C* **115**, 1311 (2011).

- [20] A. Muñoz, C. de la Calle, J. A. Alonso, P. M. Botta, V. Pardo, D. Baldomir, and J. Rivas, *Phys. Rev. B* **78**, 054404 (2008).
- [21] H. Taguchi, M. Shimada, and M. Koizumi, *J. Solid State Chem.* **29**, 221 (1979).
- [22] Q. Lu, and B. Yildiz, *Nano Lett.* **16**, 1186 (2016).
- [23] C. Mitra, T. Meyer, H. N. Lee, and F. A. Reboredo, *J. Chem. Phys.* **141**, 084710 (2014).
- [24] Q. Zhang, X. He, J. Shi, N. Lu, H. Li, Q. Yu, Z. Zhang, L.-Q. Chen, B. Morris, Q. Xu, P. Yu, L. Gu, K. Jin, and C.-W. Nan, *Nat. Commun.* **8**, 2156 (2017).
- [25] H. Jeen, W. S. Choi, J. W. Freeland, H. Ohta, C. U. Jung, and H. N. Lee, *Adv. Mater.* **25**, 3651 (2013).
- [26] H. Jeen, W. S. Choi, M. D. Biegalski, C. M. Folkman, I. C. Tung, D. D. Fong, J. W. Freeland, D. Shin, H. Ohta, M. F. Chisholm, and H. N. Lee, *Nat. Mater.* **12**, 1057 (2013).
- [27] A. Khare, D. Shin, T. S. Yoo, M. Kim, T. D. Kang, J. Lee, S. Roh, I.-H. Jung, J. Hwang, S. W. Kim, T. W. Noh, H. Ohta, and W. S. Choi, *Adv. Mater.* **29**, 1606566 (2017).
- [28] J. R. Petrie, C. Mitra, H. Jeen, W. S. Choi, T. L. Meyer, F. A. Reboredo, J. W. Freeland, G. Eres, and H. N. Lee, *Adv. Funct. Mater.* **26**, 1564 (2016).
- [29] N. Lu, P. Zhang, Q. Zhang, R. Qiao, Q. He, H.-B. Li, Y. Wang, J. Guo, D. Zhang, Z. Duan, Z. Li, M. Wang, S. Yang, M. Yan, E. Arenholz, S. Zhou, W. Yang, L. Gu, C.-W. Nan, J. Wu, Y. Tokura, and P. Yu, *Nature (London)* **546**, 124 (2017).
- [30] B. Cui, C. Song, F. Li, X. Y. Zhong, Z. C. Wang, P. Werner, Y. D. Gu, H. Q. Wu, M. S. Saleem, S. S. P. Parkin, and F. Pan, *Phys. Rev. Appl.* **8**, 044007 (2017).
- [31] See Supplemental Material at <http://link.aps.org/supplemental/10.1103/PhysRevMaterials.3.045801> for experimental details, AFM results, XRD of SCO/STO films, enlarged images of {002} peaks, details for lattice parameter calculation, RSMs of (110) SCO/LSAT film, RSMs of (111) SCO/LSAT film, variation of integer peaks, variation of surface morphology, surface morphology in different areas, and anisotropic transport behavior of (110) SCO/STO film.
- [32] H. Fujisawa, S. Seto, S. Nakashima, and M. Shimizu, *Jpn. J. Appl. Phys.* **54**, 10NA06 (2015).
- [33] H. Boschker, M. Mathews, E. P. Houwman, H. Nishikawa, A. Vailionis, G. Koster, G. Rijnders, and D. H. A. Blank, *Phys. Rev. B* **79**, 214425 (2009).
- [34] A. Geddo Lehmann, F. Congiu, N. Lampis, F. Miletto Granozio, P. Perna, M. Radovic, and U. Scotti di Uccio, *Phys. Rev. B* **82**, 014415 (2010).
- [35] W. Prellier, A. Biswas, M. Rajeswari, T. Venkatesan, and R. L. Greene, *Appl. Phys. Lett.* **75**, 397 (1999).
- [36] J. Mefford, X. Rong, A. Abakumov, W. Hardin, S. Dai, A. Kolpak, K. Johnston, and K. Stevenson, *Nat. Commun.* **7**, 11053 (2016).
- [37] L. Balcells, M. Paradinas, N. Baguès, N. Domingo, R. Moreno, R. Galce, M. Walls, J. Santiso, Z. Konstantinovic, A. Pomar, M. Casanove, C. Ocal, B. Martínez, and F. Sandiumenge, *Phys. Rev. B* **92**, 075111 (2015).
- [38] C. Yanga, B. Liua, G. Liua, F. Diaoa, H. Yangb, and Y. Wanga, *Solid State Ion.* **319**, 28 (2018).
- [39] N. F. Mott, *Conduction in Non-Crystalline Materials* (Clarendon, Oxford, 1993).
- [40] D. Yu, C. Wang, B. L. Wehrenberg, and P. Guyot-Sionnest, *Phys. Rev. Lett.* **92**, 216802 (2004).
- [41] S. Srinath, M. M. Kumar, M. L. Post, and H. Srikanth, *Phys. Rev. B* **72**, 054425 (2005).
- [42] N. Biškup, A. de Andrés, J. L. Martinez, and C. Perca, *Phys. Rev. B* **72**, 024115 (2005).